Drop impact and capture on a thin flexible fiber

Journal Name

ARTICLE TYPE

Cite this: DOI: 10.1039/xxxxxxxxxx

Received Date
Accepted Date

DOI: 10.1039/xxxxxxxxxx

www.rsc.org/journalname

Drop impact and capture on a thin flexible fiber†

Jean Comtet,*[a] Bavand Keshavarz,[a] and John W.M. Bush[b]

When a drop impacts a thin fiber, a critical impact speed can be defined, below which the drop is entirely captured by the fiber, and above which the drop pinches-off and fractures. We discuss here the capture dynamics of both inviscid and viscous drops on flexible fibers free to deform following impact. We characterize the impact-induced elongation of the drop thread for both high and low viscosity drops, and show that the capture dynamics depends on the relative magnitudes of the bending time of the fiber and deformation time of the drop. In particular, when these two timescales are comparable, drop capture is less prevalent, since the fiber rebounds when the drop deformation is maximal. Conversely, larger elasticity and slower bending time favor drop capture, as fiber rebound happens only after the drop has started to recoil. Finally, in the limit of highly flexible fibers, drop capture depends solely on the relative speed between the drop and the fiber directly after impact, as is prescribed by the momentum transferred during impact. Because the fiber speed directly after impact decreases with increasing fiber length and fiber mass, our study identifies an optimal fiber length for maximizing the efficiency of droplet capture.

1 Introduction.

The interaction of droplets with slender structures is ubiquitous in both nature and technology. In applications such as fog harvesting[1] and air filtration[2,3], forcing aerosols through fiber arrays allows for partial recovery of the liquid phase. Such recovery mechanisms can also be found in nature: plants like desert grass[4] and cactii[5] can efficiently harvest fog droplets, as can spider webs[6]. The interaction of droplets with flexible fibers also arises on the integument of insects, and so is critical for the sustenance of life at the millimeter scale[7]; for example, rain droplets can have dramatic consequences on the flight of mosquitos[8]. Slender structures and fibers are often deformable; nevertheless, the influence of structure flexibility on the capture of droplets has received very little attention.

The problem of drop impact on thin elongated structures, namely rods or fibers, was first examined by Hung and Yao[9] and Patel et al.[10]. Lorenceau et al. quantified the critical velocity threshold between capture and fragmentation for inviscid droplets impacting a fixed fiber (Figs. 1b; 2)[11]. For inviscid drops, V^* was shown to depend on the relative size of the drop and fiber, and to increase when the impact occurs on an inclined fiber[12]. Numerous other studies have been devoted to the optimization of fog harvesting structures, via alteration of mesh geometry[13], surface chemistry[14–16] and fiber microstructure[5,6,17,18], with little attention being given to the initial capture stage.

To the best of our knowledge, the influence of fiber flexibility on the efficiency of capture of impacting droplets has yet to be considered. It is well-known that droplets can significantly alter the equilibrium shape of thin fibers even in static situations[19,20]. In many cases of man-made and natural structures, the deformability of the structure may also play a critical role in droplet capture. Indeed, flexible substrates[21] and membranes[22,23] have been shown to delay or reduce splashing and jetting during drop impact, and can also significantly alter the drop fragmentation dynamics[24]. Flexible beams have been used to measure forces of impacting drops[25] and the surface chemistry of the beams has a significant impact on energy transfer during impact[26]. In most of these studies, structural flexibility seems to act as a damper; however, it may also act to feed energy back into the system, as may arise during drop impact and fragmentation on plant leaves[24].

We first describe the relevant timescales and lengthscales at play during impact, and how they are expected to interact. We then consider the impact of a drop on a rigid fiber and study the resulting dynamics for both high and low viscosity drops. Finally, we consider the role of fiber flexibility on droplet capture.

2 Physical Picture.

We consider here the effects of fiber flexibility and fluid viscosity on drop capture. Fig. 1a presents the typical impact configuration, where droplets of radius R, density ρ, surface tension σ, volume $\Omega = 4\pi R^3/3$ and viscosity η impact with velocity V on the tip of a fiber of length l and radius a, clamped at one end and free to bend at the other.

[a] Department of Mechanical Engineering, Massachusetts Institute of Technology, Cambridge, MA 02138, USA. *E-mail: jean.comtet@gmail.com
[b] Department of Mathematics, Massachusetts Institute of Technology, Cambridge, MA 02138, USA

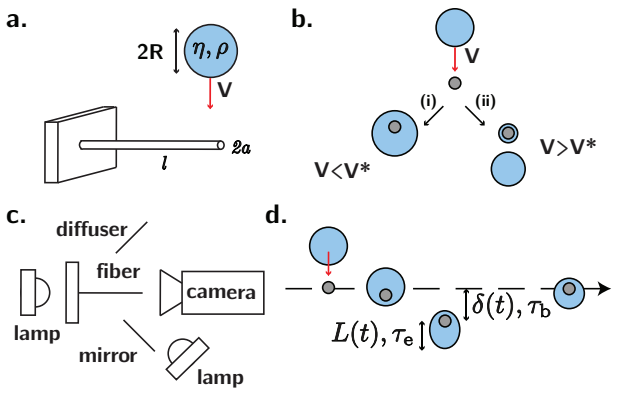

Fig. 1 (a) Typical impact configuration. A drop of radius R, viscosity η, and density ρ impacts the tip of a fiber of radius a and length l, clamped at one end. The fiber may deform in response to impact. **(b)** For a centered impact at speed V, a critical capture speed V^* can be defined. **(i)** When $V < V^*$, the drop elongates, recoils and gets caught on the fiber. **(ii)** When $V > V^*$, the drop pinches off and fractures. **(c)** Schematic of the experimental set-up, with the high-speed camera and two hallogen lamps. A mirror allows the simultaneous observation of both front and side views of the impact. **(d)** When the fiber is free to bend under impact, it is deflected by a typical distance $\delta(t)$ over a characteristic bending time τ_b, while the drop deforms an amount $L(t)$ over a characteristic elongation time τ_e.

We consider the limit where the fiber radius is small relative to drop radius, and restrict ourselves to the case for which the center of mass of the drop is aligned with the center of the fiber before impact (Fig. 1b). This configuration allows us to define a critical capture speed[11], which we denote by V^*. For impact speeds $V < V^*$, the drops will be caught on the fiber (i), and for $V > V^*$, the drops will fracture and pinch-off (ii). Fig. 2 shows typical impact sequences for the case of (i) capture and (ii) fracture. The fiber can substantially deform during impact, thus potentially playing an important role in the capture process in general and the critical impact speed V^* in particular. Changing the fiber length l allows us to systematically change the elastic response of the fiber. In the case of droplet capture, the drop hangs below the fiber, at an equilibrium offset length $L_{eq} \sim \rho g R^4/\sigma a$ set by a balance between surface tension and drop weight. In the case of droplet fracture, some fraction of the drop remains on the fiber.

We first consider the case of a rigid fiber. As the drop hits the fiber, one expects inertia and gravity to favor drop fracture and escape; viscosity and surface tension to favor capture. The relative magnitudes of the two capture forces is prescribed by the Ohnesorge number, which we define here as $Oh = 3\eta/\sqrt{\rho\sigma R}$ (where the factor 3 is Trouton's ratio and characterizes the extensional viscosity of a thread), while the relative magnitude of the forces favoring escape and fracture is characterized by the Froude number $Fr = V^2/gR \gtrsim 1$. Following impact, the drop elongates to a length $L(t)$ over a characteristic elongation timescale τ_e (Fig. 1d; Fig. 2, third frame). For $Oh \ll 1$, one expects τ_e to correspond to a typical inertia-capillary timescale $\tau_{ic} \sim \sqrt{\rho R^3/\sigma}$; when $Oh \gg 1$, one expects τ_e to correspond to the timescale of viscous momentum diffusion in the drop $\tau_v = \rho R^2/3\eta$, and drop recoil to arise over the typical viscocapillary time $\tau_{vc} = 3\eta R/\sigma$. Relevant timescales in the impact process are summarized in Table 1.

We then consider drop impact on flexible fibers. Upon impact, we expect the fiber to deform by an amount prescribed by the transfer of momentum between the drop and the fiber during impact over a typical natural bending time $\tau_b \approx l^2\sqrt{\rho_f \pi a^2/EI}$ with l the fiber length, ρ_f its density, E the Young modulus, a the fiber radius and I the area moment of inertia. Since fiber bending stores elastic energy, one expects that capture should in general be favored. However, as we shall see, elasticity may also feed energy back into the system at a critical time, thereby encouraging droplet fracture.

Table 1 Relevant Timescales

Convective time	τ_c	R/V	
Inertio-capillary time	τ_{ic}	$\sqrt{\rho R^3/\sigma}$	
Viscous diffusion time	τ_v	$\rho R^2/3\eta$	
Visco-capillary time	τ_{vc}	$\tau_{ic}^2/\tau_v = 3\eta R/\sigma$	
Bending time	τ_b	$\tau_b = l^2\sqrt{\rho_f \pi a^2/EI}$	
Ohnesorge number $Oh = 3\eta/\sqrt{\rho\sigma R}$		$Oh \ll 1$	$Oh > 1$
Elongation time	τ_e	τ_{ic}	τ_v
Recoil time	τ_r	τ_{ic}	τ_{vc}

3 Experiments

3.1 Experimental Method

A schematic of the experimental set-up is presented in Figs. 1a and 1c. Small droplets of radius R between 0.75 and 1 mm are dropped from a syringe placed above the fiber. For each experimental condition, the height is gradually adjusted to determine the velocity threshold V^*, defined in Fig. 1b, below which the entire drop is captured. Impact speeds are measured via video analysis. A mirror placed at 45° to the fiber axis, allows for the simultaneous observation of both the front and side views of the impact using a single high-speed camera Phantom Miro 320S. A typical impact sequence is shown in Fig. 2. We used frame rates up to 18,000 images per second and a typical exposure time between 5 and 50 μs. The fluids used were silicon oils of viscosity ranging from 1 to 800 cPs, with density $\rho = 970$ kg/m^3, and surface tension $\sigma = 21$ mN/m. These oils completely wet the fiber. Fibers are made of nitinol, with fiber lengths ranging from 5 to 150 mm, allowing us to tune their elastic response. For lengths longer than a few centimeters, the fibers bend under their own weight. In this case, we alter the tilt angle of the substrate so that impact always occurs on a horizontal fiber tip. Impacts occur 2-3 drop radii from the fiber tip, so that the local geometry of impact is effectively the same for all experiments. Image analysis was carried out using ImageJ.

3.2 Capture on a fixed fiber

We first consider the case of stiff fibers and investigate the influence of liquid viscosity on the droplet capture process. A fiber of radius $a = 127$ μm is clamped at both edges so that fiber flexibility does not play a role (inset, Fig. 3). Droplets of fixed radius $R = 850$ μm are dropped from a nozzle placed directly above the fiber, at heights ranging from 1 mm to 1 meter. We plot in Fig. 3 the dependence of the critical capture speed V^* on the drop vis-

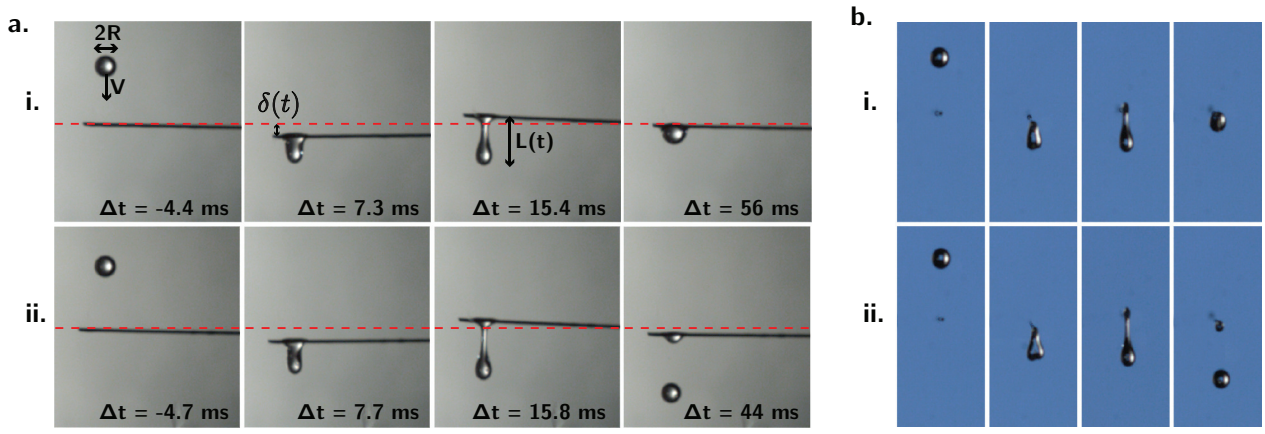

Fig. 2 Side **(a)** and front **(b)** view of the typical impact sequence of a drop of radius $R = 752$ µm on a fiber of radius $a = 127$ µm and length $l = 4.5$ cm. The horizontal dotted red line represents the equilibrium position of the fiber tip. In this sequence, the fiber is deflected by a distance $\delta(t)$, first downward (red arrow on 2nd frame) and then upward (red arrow on 3rd frame). Upon impact, the drop is stretched by an amount $L(t)$. **(i)** For impact speeds smaller than the critical capture speed (V = 0.846 m/s $< V^*$), the drop is captured. **(ii)** For $V = 0.922$ m/s $> V^*$, the drop pinches-off and fractures.

cosity (lower axis) and the Ohnesorge number $Oh = 3\eta/\sqrt{\rho\sigma R}$ that characterizes the relative importance of viscous and capillary forces in the capture process (upper axis). For low Oh, V^* is independent of viscosity, consistent with the inviscid case described by Lorenceau et al.[11] (horizontal dotted line, Fig. 3). The over-estimation of the critical capture speed by the model could result from the drop radius being close to the maximal radius of static drops on fibers. For $Oh > 1$, the capture threshold increases linearly with fluid viscosity, indicating that viscous dissipation favors droplet capture. In this case, the critical speed V^* is prescribed by a balance between inertial and viscous effects. Specifically, we expect viscous stresses to overcome drop inertia when $\rho V^2/R \sim 3\eta V/R^2$. Defining the Reynolds number as $Re \approx \frac{\rho RV}{3\eta}$, our experiments indicate a capture threashold of $Re \approx 1.8$. This condition can equivalently be deduced by balancing the drop convective time R/V with the viscous diffusion time $\tau_v = \rho R^2/3\eta$.

To understand the dynamics of impact, we show in Fig. 4 the typical elongation dynamics of drops impacting fibers in the two limits $Oh \ll 1$ and $Oh > 1$. Following impact, the drop is stretched and elongates over a typical elongation timescale τ_e, before either (i) recoiling over a time τ_r or (ii) fracturing. For $Oh \ll 1$, the elongation dynamics is symmetric, as both elongation time τ_e and recoil time τ_r scale as the typical inertia-capillary or Rayleigh timescale $\tau_{ic} \sim \sqrt{\rho R^3/\sigma}$. When $Oh \gg 1$, the drop speed is first reduced over a viscous timescale $\tau_v = \rho R^2/3\eta$; the thread then recoils with a characteristic visco-capillary time $\tau_{vc} = 3\eta/\sigma R$. In this case, the elongation dynamics is highly asymmetric, as the ratio between the recoil and elongation times, τ_r/τ_e scales as $Oh^2 > 1$.

3.3 Fiber deformation upon impact

We now study the case where the fiber is free to bend and deform in response to impact. We use fibers of radius $a = 127$ μm and $a = 63.5$ μm. When studying impacts of low viscosity drops ($Oh \ll 1$), we increased the radius of the outer extremity of the fiber to 215 μm, allowing for larger capture speeds that could be

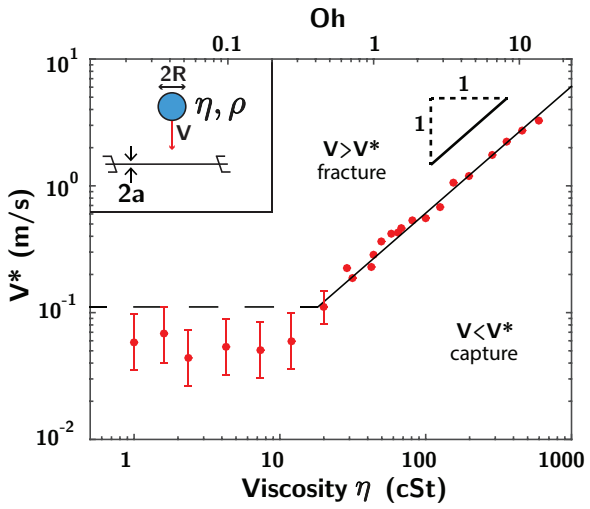

Fig. 3 Impact on a rigid fiber (inset). Variation of the critical capture speed V^* (m/s) with drop viscosity η (lower axis) and Ohnersorge number $Oh = 3\eta/\sqrt{\rho\sigma R}$ (upper axis). The dashed line is the expected capture speed for $Oh \ll 1$ using the expression from Lorenceau et al.[11]. For $Oh \geq 1$, V^* increases linearly with viscosity. Drop radius is $R = 850$ µm and fiber radius $a = 127$ µm. Error bars characterize the uncertainty in the impact speed prevalent at low speeds.

measured more precisely. The typical time evolution of the fiber (red) and the drop (green) deformations following impact are shown in Fig. 5a. We denote by $\delta(t)$ the fiber displacement, and $L(t)$ the drop elongation relative to the fiber.

3.3.1 Fiber oscillations

Following impact, the fiber starts to oscillate with a characteristic time scale τ_b (Fig. 5a). In Fig. 5b, we plot the variation of this bending timescale τ_b with fiber length l and find $\tau_b \sim l^2$, as is consistent with the natural bending time of a free beam :

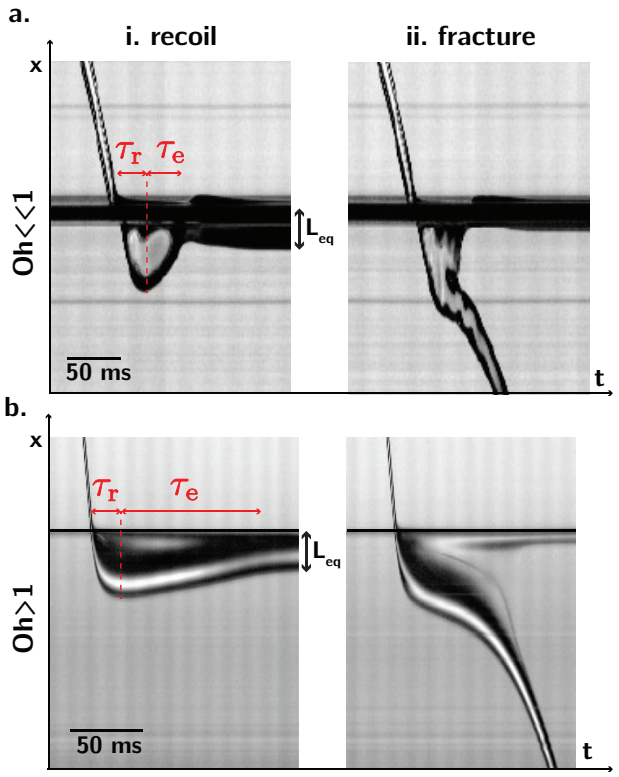

Fig. 4 Kymograph (spatiotemporal diagrams) of impact on a rigid fiber. Vertical slices of video images of 1 pixel width passing through the drop centerline are placed side by side with time increasing from left to right. **(a)** $\eta = 1$ cPs ($Oh << 1$) and **(b)** $\eta = 190$ cPs ($Oh > 1$). The drop elongates for a time τ_e, and then either (i) recoils over a time τ_r to its equilibrium offset length L_{eq}, or (ii) fractures. For $Oh \ll 1$, $\tau_e \sim \tau_r$ is set by the inertia-capilary time $\tau_{ic} \sim \sqrt{\rho R^3/\sigma}$, while for $Oh > 1$, $\tau_e \sim \rho R^2/3\eta$ and $\tau_r \sim 3\eta R/\sigma$ (Cf. Table 1).

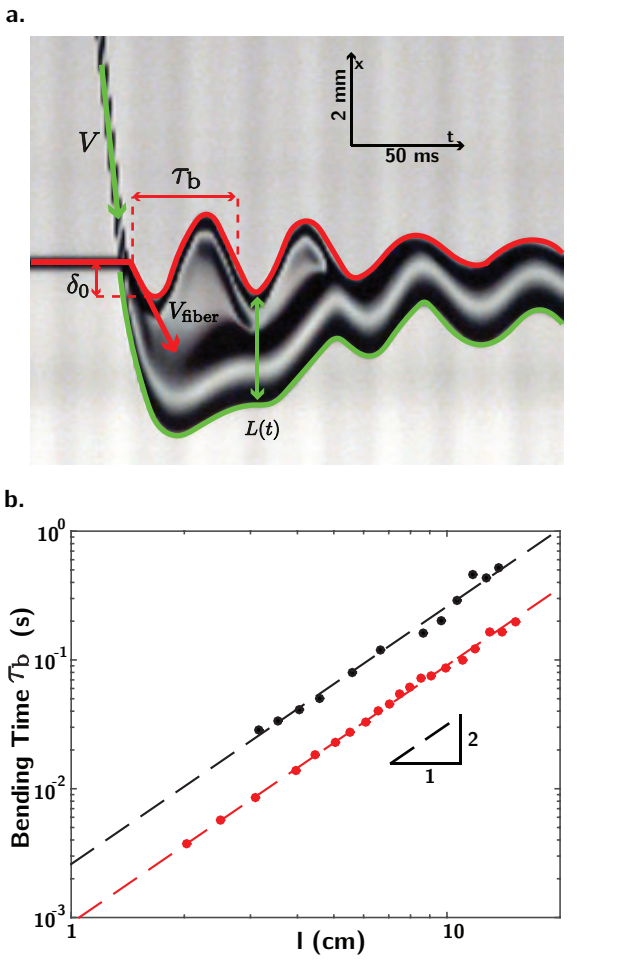

Fig. 5 Impact on a flexible fiber. **(a)** Kymograph for the impact of a viscous drop ($\eta = 100$ cst) of speed V on a fiber of radius $a = 127$ µm and length $l = 5$ cm. The fiber starts oscillating with a typical timescale τ_b, amplitude δ_0 and initial velocity V_{fiber}. **(b)** Variation of the typical bending timescale τ_b with fiber length L. We find $\tau_b \sim l^2$, as expected on the basis of Eq. (1). Black points: impacts for $Oh \ll 1$, with a = 63.5 µm and a fiber tip of 250 µm. Red points: impacts for $Oh > 1$, with a = 127 µm.

$$\tau_b = \frac{2\pi}{\beta^2}\sqrt{\frac{\rho_f \pi a^2}{EI}}l^2 \qquad (1)$$

where $\beta = 1.875$ for the first mode of oscillation, $E = 64$ GPa the beam's Young Modulus, $I = \pi a^4/4$ the moment of inertia, $\rho_f = 6450$ kg/m^3 the beam density. This scaling is consistent with the fact that drop weight can be neglected compared to fiber weight, and does not affect the oscillatory dynamics of the fiber. We note that for the longest fibers, higher modes of vibration are also excited, but the timescale of the first mode remains dominant (see e.g. Fig. 8c). While fiber oscillations are damped, the drop capture or fracture occurs during the initial oscillations of the fiber; consequently, we may safely neglect this damping.

3.3.2 Initial fiber speed

The two other critical parameters for impact on flexible fibers are the oscillation amplitude δ_0 after impact (red curve, Fig. 5a), and the initial fiber speed V_{fiber} directly after impact (red arrow, Fig. 5a). Neglecting higher modes of oscillation and fiber damping, we express the fiber displacement $\delta(t)$ as:

$$\delta(t) = \delta_0 \sin(2\pi t/\tau_b) = \frac{V_{fiber}\tau_b}{2\pi}\sin(2\pi t/\tau_b) \qquad (2)$$

where $V_{fiber} = \dot{\delta}(0) = 2\pi\delta_0/\tau_b$. In Figs. 6a and c we plot V_{fiber} as a function of the drop impact speed V. We find markedly different behaviour, according to the drop viscosity. For low viscosity drops (Fig. 6a), the initial fiber speed is largely independent of drop impact speed for impacts leading to fracture (black points). Conversely, for viscous drops, initial fiber speed is proportional to drop impact speed (Fig. 6c).

To rationalize this behaviour, let us consider the processes accompanying impact. Because convection time R/V is typically small relative to the fiber response time τ_b, fiber elasticity can be neglected when considering the impact dynamics[25], and we can express the transfer of momentum between the drop and the fiber during impact as follows:

$$M_{eff}V_{fiber} \sim F\Delta t \qquad (3)$$

where M_{eff} is the effective fiber mass, F the force applied by the drop to the fiber and Δt the interaction time. Considering clamped

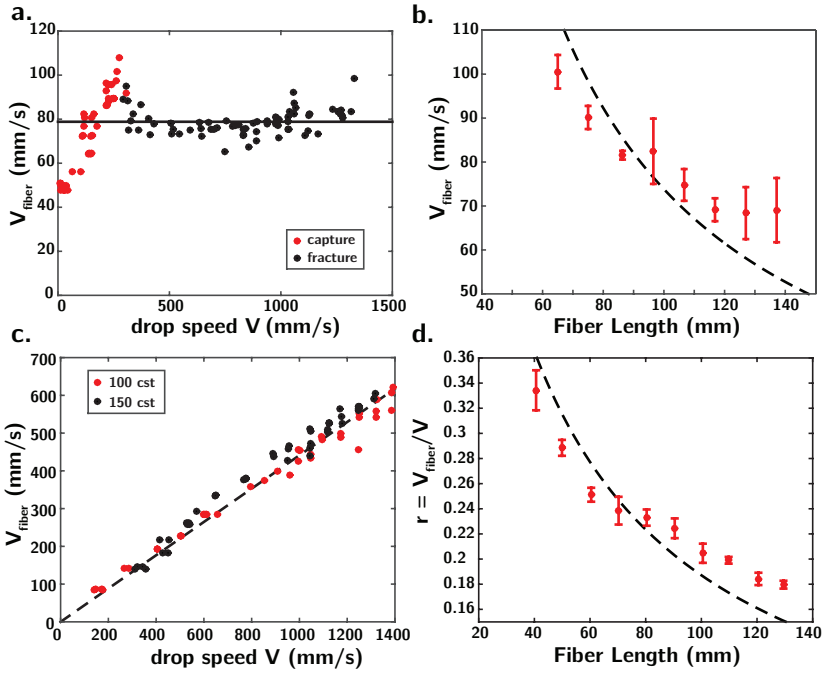

Fig. 6 Momentum transfer during impact. Variation of post-impact initial fiber speed V_{fiber} with drop impact speed V. **(a-b)** Low viscosities drops ($\eta = 1$ cPs), fiber radius is a = 63.5 µm and radius of the fiber tip is 215 µm. **(a)** Fiber length l is 8 cm. For impact speeds leading to drop fracture (black points), V_{fiber} is independent of drop impact speed V. **(b)** V_{fiber} decreases with increasing fiber length and fiber mass, according to Eq. (4). **(c-d)** High viscosities drops ($\eta > 100$ cPs), fiber radius is $a = 127$ µm. **(c)** V_{fiber} is proportional to V and independent of liquid viscosity. Fiber length is 60 µm. **(d)** The coefficient of proportionality $r = V_{\text{fiber}}/V$ decreases with increasing fiber length according to Eq. (5). In **(b)** and **(d)**, error bars correspond to one typical standard deviation. The dashed lines are fits to the data points (see text for details).

boundary conditions and impact on the tip, the effective fiber mass is $\rho_f \pi a^2 l/3$, with l the fiber length, a the fiber radius and ρ_f the fiber density[25]. For simplicity, we take $F \sim \eta RV$ in both low and high viscosity limits.

For low viscosities, when the impact speed is too large for the drop to be caught on the fiber, the drop crosses the fiber with a contact time $\Delta t \sim 2R/V$ inversely proportional to the impact speed. Rewriting Eq. (3), this condition predicts an initial fiber speed independent of the drop impact speed, as is apparent in the black points of Fig. 6a:

$$V_{\text{fiber}} \sim \frac{\eta R^2}{M_{\text{eff}}} \tag{4}$$

As expected from Eq. (4), V_{fiber} decreases with increasing fiber length, that is, larger effective fiber mass M_{eff} (Fig. 6b). The dashed line in Fig. 6b is the best fit to the experimental points, using the expression $V_{\text{fiber}} \approx \alpha \cdot 8\pi\eta(2R)^2 V/(\rho_f \pi a^2 l/3)$, with $\alpha \approx 3$ a fitting parameter. For the lowest impact speeds, where the drop is captured by the fiber (Fig. 6a, red points), Eq. (4) breaks-down due to an increase in the interaction time between the fiber and the drop, which leads to enhanced momentum transfer. In this case, for which $\Delta t \approx \tau_{\text{ic}}$, fiber speed is expected to grow linearly with drop impact speed: $V_{\text{fiber}} \sim \eta RV/M_{\text{eff}} \cdot \sqrt{\rho R^3/\sigma}$ (Fig. 6a, red points).

For large viscosities, whether impact leads to capture or fracture, the drop initially "sticks" to the fiber, transfering momentum to the fiber for a time $\Delta t \sim \rho R^2/3\eta$ corresponding to the characteristic time of viscous penetration of the drop on the fiber. Rewriting equation (3), we obtain:

$$V_{\text{fiber}} \sim \frac{\rho R^3 V}{M_{\text{eff}}} \tag{5}$$

In this regime, the initial fiber speed for both capture and fracture is proportional to the drop impact speed, and momentum transfer is independent of viscosity, as is evident in Fig. 6c. Eq. (5) can also be understood by assuming an inelastic collision between the drop and fiber, which leads to $(m + M_{\text{eff}})V_{\text{fiber}} \sim mV$ where $m \sim \rho R^3$ is the drop mass. We denote by $r = V_{\text{fiber}}/V$ the relative magnitudes of these two velocities. As expected from Eq. (5), r decreases with increasing fiber length, or equivalently increasing fiber mass M_{eff} (Fig. 6d). The dashed line in Fig. 6d is the best fit to the experimental points, using the expression $r \approx 1/(1 + \beta \cdot \rho_f \pi a^2 l/(4\pi\rho R^3))$, with $\beta \approx 4$ a fitting parameter.

3.4 Capture on a flexible fiber

With this physical picture in mind, we now study how the capture criteria for drops changes with fiber elasticity. We report in Fig. 7 the variation of the critical capture velocity V^* with fiber flexibility, for both small (7a) and large (7b) Ohnesorge numbers as a function of the ratio of bending to elongation times τ_b/τ_e, which necessarily increases with fiber flexibility. The black horizontal dashed line indicates the capture speed in the limit of rigid fibers, which we denote by V_0^*. We recall that for $Oh \ll 1$, the elongation time τ_e scales as the inertio-capillary time of the drop

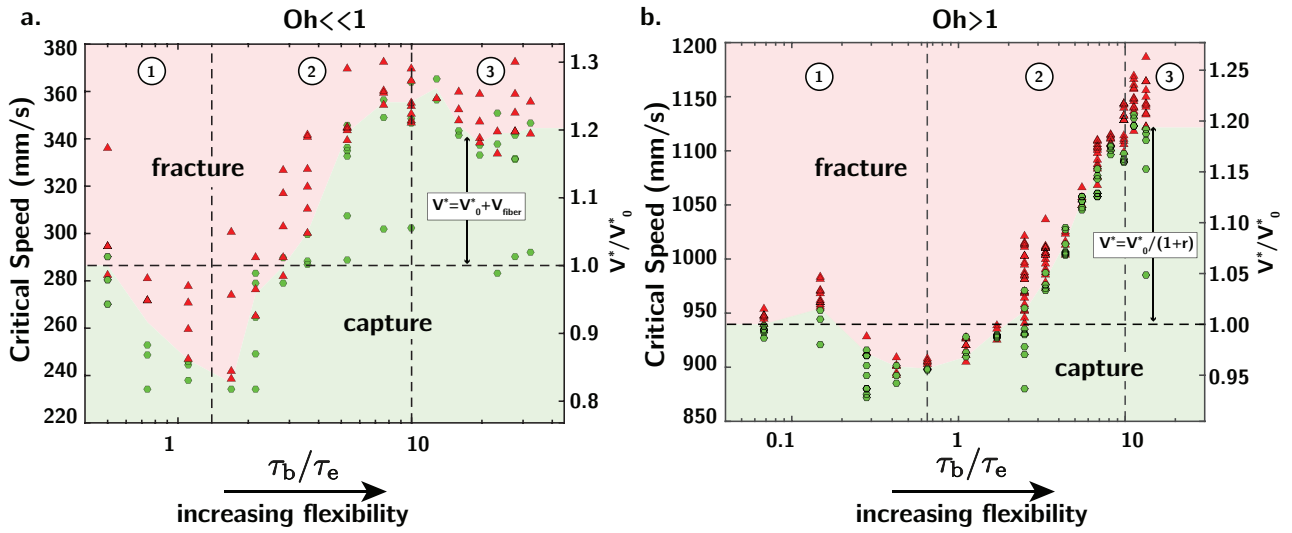

Fig. 7 Variation of critical capture speed V^* with τ_b/τ_e, the ratio of bending and elongation timescales. The horizontal dashed line represents the experimentally determined capture speed on a rigid fiber V_0^*. Red triangles: impacts leading to fracture. Green dots : impacts leading to capture. **(a)** For $Oh \ll 1$, $\tau_e = \sqrt{\rho R^3/\sigma} \approx 15 \pm 1.5$ ms. **(b)** For $Oh > 1$, $\tau_e = \rho R^2/3\eta \approx 13.5 \pm 1.5$ ms. In zone 1, the critical capture speed V^* decreases with increasing flexibility, being uniformly less than the capture speed on rigid fibers V_0^*. Increasing flexibility then leads to larger capture speeds (zone 2), $V^* > V_0^*$, up to a point where V^* tends to plateau (zone 3). Drop radius R is 820 µm. In the low viscosity case **(a)**, V_0^* is within 10% of the expression predicted by Lorenceau et al.

$\tau_{ic} = \sqrt{\rho R^3/\sigma}$ (Fig. 4a), while for $Oh \gg 1$, τ_e scales as the viscous timescale $\tau_v \sim \rho R^2/3\eta$ (Fig. 4b).

To understand the phase diagrams of Fig. 7 in term of the interaction of the drop and fiber, we present in Fig. 8 typical kymographs of capture events for $Oh \gg 1$. For short fibers (Fig. 8a), small fiber oscillations arise over a characteristic time τ_b short relative to the characteristic elongation time τ_e of the drop. In this limit we expect to recover the static critical capture condition (Fig. 8a, $\tau_b < \tau_e, V^* \approx V_0^*$). As fiber flexibility increases, we observe a decrease in the critical capture speed (Fig. 7, zone 1), which reaches a minimum when the elongation and bending timescales are of the same order. In this critical case, the deformed fiber begins to rebound just as the drop is reaching its maximal length, thus precipitating fracture at a speed lower than in the static fiber case (Fig. 8b, $\tau_b \sim \tau_e$, $V^* < V_0^*$). Thereafter, V^* then increases progressively with flexibility, and exceeds that on a stiff fiber V_0^* (Fig. 7, zone 2). In this regime, some of the kinetic energy of impact is stored as elastic energy by the fiber, and is restored as the drop recoils ($\tau_b > \tau_e$, $V^* > V_0^*$).

Finally, for long fibers, or large bending period (Fig. 8c, $\tau_b \gtrsim 10 \cdot \tau_e$, Zone 3) the critical capture speed saturates. In this limit, fiber oscillations are decorrelated from the drop temporal dynamics, and the fiber is carried with the drop at its initial velocity V_{fiber}, independent of fiber flexibility (see Fig. 6). This long-fiber limit leads to a maximal increase in the capture speed; since the fiber simply follows the drop, the initial elongation rate of the drop $\dot{L}(0) = V - V_{fiber}$ can be greatly reduced relative to that arising in the static fiber case. For $Oh \ll 1$, the initial fiber speed V_{fiber} is independent of drop impact speed (Fig. 6a), and we expect the capture speed V^* to be increased by an amount V_{fiber} relative to that on a stiff fiber V_0^*. For $Oh \gg 1$, the ratio $r = V_{fiber}/V_{drop}$ is constant and we thus expect $V^* = V_0^*/(1-r)$. These two predictions are consistent with our experimental data, and show the critical importance of momentum transfer between the drop and the fiber in optimizing capture efficiency.

4 Discussion

We have investigated the dynamics of drop impact on flexible fibers, and examined how the critical capture speed depends on both drop viscosity and fiber flexibility. Surface tension and viscosity are the two forces favoring drop capture, and their relative magnitude is prescribed by an Ohnersorge number $Oh = 3\eta/\sqrt{\rho\sigma R}$. We first characterized the elongation dynamics of a drop impacting a rigid fiber for high and low Oh. For $Oh \ll 1$, we showed that the drop elongates and recoils symmetrically with a typical inertia capillary timescale $\tau_{ic} \sim \sqrt{\rho R^3/\sigma}$ (Fig. 4a). When $Oh > 1$, drop elongation is asymmetric: the thread is first damped over a viscous timescale $\tau_v = \rho R^2/3\eta$ and then recoils with characteristic viscocapillary time $\sigma R/3\eta$ (Fig. 4b). For $Oh > 1$, balancing the viscous time τ_v with the convective time R/V leads to a simple capture condition $Re \lesssim 1.8$ (Fig. 3).

When the fiber is free to bend, the impacting drop may excite oscillations of the fiber at its natural period τ_b, with an amplitude set by momentum transfer during impact (Fig. 5). For large viscosities, the impact is inelastic, and the initial fiber speed V_{fiber} is proportional to the drop speed V. For low viscosities, the contact time varies inversely with the impact speed, leading to an initial fiber speed V_{fiber} that is independent of drop speed V (Fig. 6). In both cases, momentum transfer is independent of fiber elasticity, but depends on the fiber length.

The ratio of the drop elongation timescale τ_e and the fiber bending time τ_b plays a critical role when considering capture

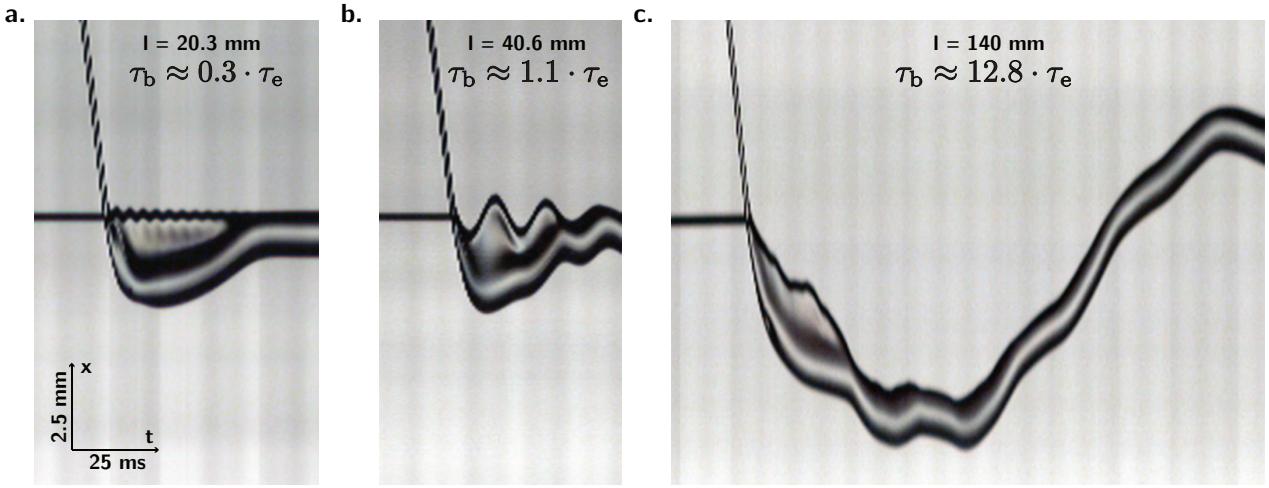

Fig. 8 Experimental kymographs for drop impact on a flexible fiber in the $Oh > 1$ case. **(a)** Short fiber. Fiber oscillations are small in amplitude and arise over a timescale short relative to the typical drop deformation time τ_e. **(b)** Intermediate flexibility. The fiber rebounds as the drop achieves its maximum deformation (Fig. 7, transition 1-2). **(c)** Long fibers. The fiber follows the drop, and rebounds only once the drop has recoiled, thus increasing the capture speed relative to the rigid-fiber case (Fig. 7, zone 3).

criteria. For both viscous and inviscid drops, the critical capture speed varies non-monotically with fiber flexibility. In particular, the capture speed V^* reaches a minimum when the fiber's bending time is comparable to the drop's elongation time, as the fiber begins to rebound just as the drop is reaching its maximal length, thus precipitating fracture. Here, the flexible structure does not act strictly as a damper, but instead promotes fragmentation.

For larger flexibility, the fiber begins to rebound only after the drop has started recoiling, leading to an increase in the critical capture speed. Beyond a critical flexibility, the fiber temporal dynamics occurs over a time much larger than the fiber elongation time, and the critical capture speed plateaus. In this limit, the fiber follows the drop with a constant speed, prescribed by the momentum transferred during impact, that decreases with increasing fiber length and fiber mass. We can thus define an optimal fiber length for capture. Specifically, we require that the bending time $\tau_b \sim l^2\sqrt{\rho_f/Ea^2}$ be large enough for fiber rebound to occur after drop recoil, and that the fiber mass $M_{\text{eff}} \sim \rho_f a^2 l$ be small enough to allow maximal momentum transfer between the drop and the fiber, thereby reducing their relative speed. The fiber radius a and Young Modulus E are thus critical parameters in attaining the regime $\tau_b \gtrsim 10 \cdot \tau_e$ while maintaining a low fiber mass ($\tau_e \approx 5$ ms for a 1 mm water drop). We note that locally increasing the radius at the point of impact allows for large momentum transfer during impact, without reducing the capture efficiency associated with large drop-to-fiber aspect ratio[11].

Droplet capture can thus be significantly enhanced by large fiber flexibility. This finding informs applications in which flexible structures are used to recover aerosols, as it provides a straightforward way to boost droplet recovery rates. Finally, we note that fiber surface chemistry and roughness will also affect criteria for droplet capture on flexible fibers, as will the detailed geometry of impact. Such effects are left for future consideration.

5 Acknowledgements

We thank Pedro Reis for providing the nitinol fibers. Jean Comtet thanks Peko Hosoi for her support.

References

1 O. Klemm, R. S. Schemenauer, A. Lummerich, P. Cereceda, V. Marzol, D. Corell, J. van Heerden, D. Reinhard, T. Gherezghiher, J. Olivier *et al.*, *Ambio*, 2012, **41**, 221–234.

2 P. Contal, J. Simao, D. Thomas, T. Frising, S. Callé, J. Appert-Collin and D. Bémer, *Journal of Aerosol Science*, 2004, **35**, 263–278.

3 T. Frising, D. Thomas, D. Bemer and P. Contal, *Chemical Engineering Science*, 2005, **60**, 2751–2762.

4 A. Roth-Nebelsick, M. Ebner, T. Miranda, V. Gottschalk, D. Voigt, S. Gorb, T. Stegmaier, J. Sarsour, M. Linke and W. Konrad, *Journal of The Royal Society Interface*, 2012, rsif20110847.

5 J. Ju, H. Bai, Y. Zheng, T. Zhao, R. Fang and L. Jiang, *Nature communications*, 2012, **3**, 1247.

6 Y. Zheng, H. Bai, Z. Huang, X. Tian, F.-Q. Nie, Y. Zhao, J. Zhai and L. Jiang, *Nature*, 2010, **463**, 640–643.

7 J. W. Bush, D. L. Hu and M. Prakash, *Advances in Insect Physiology*, 2007, **34**, 117–192.

8 A. K. Dickerson, P. G. Shankles, N. M. Madhavan and D. L. Hu, *Proceedings of the National Academy of Sciences*, 2012, **109**, 9822–9827.

9 L. Hung and S. Yao, *International journal of multiphase flow*, 1999, **25**, 1545–1559.

10 P. D. Patel, E. S. Shaqfeh, J. E. Butler, V. Cristini, J. Bławzdziewicz and M. Loewenberg, *Physics of Fluids (1994-present)*, 2003, **15**, 1146–1157.

11 É. Lorenceau, C. Clanet and D. Quéré, *Journal of colloid and interface science*, 2004, **279**, 192–197.

12 K. Piroird, C. Clanet, É. Lorenceau and D. Quéré, *Journal of colloid and interface science*, 2009, **334**, 70–74.
13 H. Andrews, E. Eccles, W. Schofield and J. Badyal, *Langmuir*, 2011, **27**, 3798–3802.
14 K.-C. Park, S. S. Chhatre, S. Srinivasan, R. E. Cohen and G. H. McKinley, *Langmuir*, 2013, **29**, 13269–13277.
15 B. S. Lalia, S. Anand, K. K. Varanasi and R. Hashaikeh, *Langmuir*, 2013, **29**, 13081–13088.
16 L. Zhai, M. C. Berg, F. C. Cebeci, Y. Kim, J. M. Milwid, M. F. Rubner and R. E. Cohen, *Nano Letters*, 2006, **6**, 1213–1217.
17 Z. Huang, Y. Chen, Y. Zheng and L. Jiang, *Soft Matter*, 2011, **7**, 9468–9473.
18 Y. Hou, Y. Chen, Y. Xue, Y. Zheng and L. Jiang, *Langmuir*, 2012, **28**, 4737–4743.
19 C. Duprat, S. Protiere, A. Beebe and H. Stone, *Nature*, 2012, **482**, 510–513.
20 S. Protiere, C. Duprat and H. Stone, *Soft Matter*, 2013, **9**, 271–276.
21 S. Mangili, C. Antonini, M. Marengo and A. Amirfazli, *Soft Matter*, 2012, **8**, 10045–10054.
22 R. E. Pepper, L. Courbin and H. A. Stone, *Physics of Fluids*, 2008, **20**, 082103.
23 J. Field, J. Dear and J. Ogren, *Journal of Applied Physics*, 1989, **65**, 533–540.
24 T. Gilet and L. Bourouiba, *Journal of The Royal Society Interface*, 2015, **12**, 20141092.
25 D. Soto, A. B. De Larivière, X. Boutillon, C. Clanet and D. Quéré, *Soft matter*, 2014, **10**, 4929–4934.
26 S. Gart, J. E. Mates, C. M. Megaridis and S. Jung, *Physical Review Applied*, 2015, **3**, 044019.